Research on Flow Rule and Thermal Dissipation Between the Rotor Poles of a Fully Air-Cooled Hydrogenerator

Shukuan Zhang, Weili Li, Jinyang Li, Likun Wang, and Xiaochen Zhang, *Member, IEEE*

Abstract—**Aiming at providing a theoretical basis for the 1000-MW giant fully air-cooled hydrogenerator, which is being studied and developed currently, this paper established a coupling calculation model of 3-D fluid and temperature field based on the actual structure and size of a 250-MW fully air-cooled fanless hydrogenerator. Fluid dynamics control equations, and corresponding boundary conditions in the solved region were given. The additional losses from electromagnetic field calculation were applied to the coupling model as heat sources. Using a computational fluid dynamics approach, the flow distribution of cooling air and the temperature distribution of rotor structures were obtained. It focused on the axial and radial variation rules of the flow condition of cooling air between adjacent poles. Meanwhile, it conducted a detailed research study on the variation rule of the heat-transfer coefficients of pole shoes and damping bars. Temperature calculated value of exciting windings was coincident well with the measured value. The calculated error between the two values meets the engineering requirement, thus verifying both applicability and accuracy of the solution method this paper presents.**

Index Terms—**Computational fluid dynamics (CFD), fluid field, heat-transfer coefficient, hydrogenerator, temperature field.**

I. INTRODUCTION

HYDROPOWER resource occupies the largest proportion in clean energy sources and enjoys the advantages of cleanliness, high efficiency, and huge exploitable capacity. Because of these advantages, many countries in the world continue to develop it on a large scale. Hydrogenerators are the most important energy conversion device in the hydropower station. If a local structure of hydrogenerators is overheated, the insulation will be damaged or the local thermal stress will increase, both of which are serious problems affecting the operation safety of the unit [1], [2].

A water-cooled or air-cooled cooling system is employed to evacuate the power losses of a hydrogenerator. Compared with the water-cooling system, the fully air-cooling system does not require an auxiliary water treatment facility. The maintenance of water leakage and clogging within a water-cooled coil is fairly complicated. Fully air-cooled cooling system is increasingly applied to large-capacity hydrogenerators since it has the advantages of high reliability and low operation and maintenance cost. However, the cooling effect of a fully air-cooled cooling system, an indirect cooling method, is not as good as the effect of a water-cooled system, which is a direct cooling method. Meanwhile, in order to avoid potential broken fault of a fan mounted on the shaft and reduce ventilation loss, which comprises 20%–40% total power losses, a fully air-cooled system without fan is more and more employed. However, there is no doubt that canceling fan will cause decrement of the total circulation air flow rate and increment of the temperature rise of stator and rotor windings, thus weakening the cooling effect conspicuously. Based on the aforementioned reasons, employing a fully air-cooled fanless cooling system will cause many problems of meeting the requirements of cooling effect. Due to the rotation of rotor poles and rotor yokes, the cooling air presents a very complex distribution in the hydrogenerator. In addition, flow condition of cooling air has direct impact on the temperature rise of various parts in the hydrogenerator; thus, an appropriate flow distribution is required. Therefore, the research on the flow rule of the cooling air in a fully air-cooled fanless hydrogenerator has the very significance in verifying the rationality of ventilation system and accurately predicting the distribution of hydrogenerator temperature field.

There have been many papers published on the research of fluid and temperature fields of electrical machines. In [3]–[7], the lumped-parameter thermal network (LPTN) is adopted to predict the temperature rise of electrical machines. Such method enjoys an advantage of fast calculation because the number of involved nodes in the computation is small; in [8], a model of 3-D nonlinear stator temperature field is established to study the impact of hydrogenerator insulation aging on the stator temperature field; in [9], the time-stepping finite-element method (FEM) is adopted to calculate the additional surface of rotor damper bars and pole shoes; in [10], the flow velocity of the fluid in the stator ventilation ducts of salient pole synchronous machine is calculated and the surface heat-transfer coefficient by the theory of fluid similarity is determined, thereby obtaining the distribution of stator temperature field; in [11], infrared thermography is used in the measurement of hydrogenerator rotor temperature; in [12]–[18], a complete overview of evolution and modern approaches in the thermal analysis of electrical machines are presented, and three

S. Zhang and J. Li are with the School of Electrical Engineering and Automation, Harbin Institute of Technology, Harbin 150001, China (e-mail: zhangshukuan@hotmail.com; jinyang_yx@163.com).

W. Li and X. Zhang are with Beijing Jiaotong University, Beijing 100044, China (e-mail: li.weili@yeah.net; xchzhang@bjtu.edu.cn).

L. Wang is with the College of Electrical and Electronic Engineering, Harbin University of Science and Technology, Harbin 150080, China (e-mail: wlkhello@163.com).

Color versions of one or more of the figures in this paper are available online at http://ieeexplore.ieee.org.

TABLE I
BASIC PARAMETERS OF THE GENERATOR

Basic Parameter	Value
Capacity (MW)	250
Voltage (V)	15750
Current (A)	10183
Power factor	0.9
Frequency (Hz)	50
Pole number	88

approaches of LPTN, FEM, and computational fluid dynamics are exemplified.

Obviously, most researchers focus on fluid and temperature field distribution within the stator region of a hydrogenerator. However, few scholars devote to the research of fluid–thermal coupling analysis within the rotor region of hydrogenerator, particularly with a fully air-cooled fanless ventilation system. In this paper, a 3-D fluid–thermal coupling calculation model of a 250-MW fully air-cooled hydrogenerator rotor is established and flow condition of cooling air, as well as temperature distribution of various structures, is obtained. Axial and radial distribution rules of cooling air between adjacent poles are analyzed in detail. Meanwhile, it conducts a research study on the heat-transfer coefficient of pole shoes and damping bars. The accuracy of calculated results is verified by a comparison between the temperature calculated value of exciting windings and the measured value, providing a theoretical basis for the 1000-MW giant fully air-cooled hydrogenerator of the largest single unit capacity developed currently.

II. COUPLING MODEL OF THREE-DIMENSIONAL FLUID AND TEMPERATURE FIELDS

A. Ventilation Structure and Establishment of Physical Model

The investigated machine in this paper is a 250-MW fully air-cooled fanless hydrogenerator, and its basic parameters are illustrated in Table I. The model this paper establishes adopts a self-circulation dual-path fanless ventilation system. Such kind of ventilation system makes use of the pressure head effect of rotor support and rotor yoke and cancels the fans in order to greatly reduce the ventilation loss.

Fig. 1 is a diagram for its ventilation and cooling system. The cooling air from the heat exchanger (path 1–①) first flows through stator end windings (path 1–②), cools the stator end windings, and then flows into the upper (for path 1) ventilation channel (path 1–③). Along the path ④–⑥–⑦, a part of cooling air flows through the rotor support into the rotor yoke ventilation ducts, and then through the fluid region between adjacent poles to cool the exciting windings; along the path ③–⑤, the other part of cooling air flows into the end fluid region by a horizontal disc air deflector. The air from the two paths radially flows into the air gap after convergence, cools armature winding and stator core through the stator radial ventilation ducts ⑧, and then re-enter the heat exchanger to dissipate heat. The upper and lower ventilation paths are symmetric, thus constituting a dual-path cooling system. Cooling air takes the
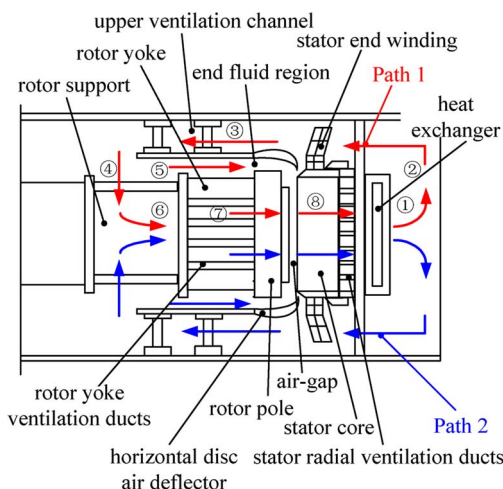

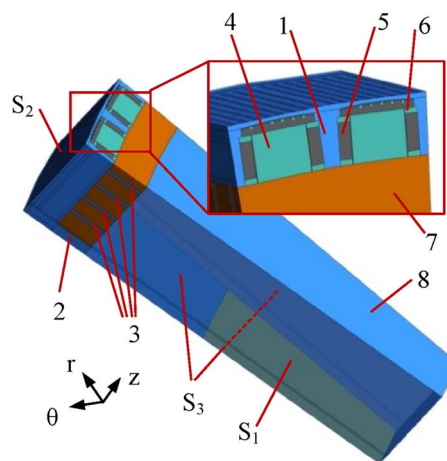Fig. 1.　Ventilation system structure diagram.

Fig. 2.　Solved region of coupling model. (1) Fluid region between adjacent poles. (2) End fluid region. (3) Rotor yoke ventilation duct. (4) Poles. (5) Exciting windings. (6) Exciting winding support plate. (7) Yoke. (8) Rotor support. (S1) Velocity inlet. (S2) Pressure outlet. (S3) Adiabatic surfaces.

heat away, which is generated by exciting windings, armature windings, and other heating structures.

Based on the actual size and structure of the motor, a 3-D fluid–thermal coupling model is established in this paper. The region of calculation model includes half length of the prototype in the axial direction and a pair of rotor poles in the circumferential direction according to symmetry of the rotor structure. As illustrated in Fig. 2, the calculation model includes solid regions and fluid regions. The solid regions represent rotor structures such as a pair of poles, damper bars, exciting windings, supporting plates, pole pressure plates, and rotor yoke. The fluid regions (see the blue part in Fig. 2) represent the area where cooling air flows such as four rotor ventilation ducts, the region between adjacent poles, and so on, where r represents the radial direction, θ represents the circumferential direction, and z represents the axial direction.

B. Mathematical Model and Boundary Conditions

The ventilation system of a fully air-cooled hydrogenerator has a complex structure, and the cooling air with high Reynolds
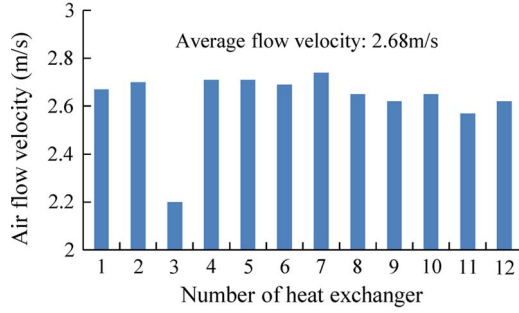
Fig. 3.   Measured value of air flow velocity.

number is in a turbulent state. Meanwhile, the cooling air in the model could be treated as an incompressible fluid. Based on fluid dynamics and heat-transfer theory, a mathematical model is established within the solved region, which satisfies the mass conservation equation, momentum equation, and energy conservation equation [19]

$$
\begin{cases}
\frac{\partial \rho}{\partial t} + \nabla \cdot (\rho \boldsymbol{u}) = 0 \\
\frac{\partial (\rho u)}{\partial t} + \nabla \cdot (\rho \boldsymbol{u} u) = \nabla \cdot (\mu \nabla u) - \frac{\partial P}{\partial x} + S_u \\
\frac{\partial (\rho v)}{\partial t} + \nabla \cdot (\rho \boldsymbol{u} v) = \nabla \cdot (\mu \nabla v) - \frac{\partial P}{\partial y} + S_v \\
\frac{\partial (\rho w)}{\partial t} + \nabla \cdot (\rho \boldsymbol{u} w) = \nabla \cdot (\mu \nabla w) - \frac{\partial P}{\partial z} + S_w \\
\frac{\partial (\rho T)}{\partial t} + \nabla \cdot (\rho \boldsymbol{u} T) = \nabla \cdot \left(\frac{k}{c} \nabla T\right) + S_T
\end{cases}
\tag{1}
$$

where ρ is fluid density (in kilograms per cubic meter), t is time (in seconds), and $\boldsymbol{u}$ is the velocity vector of fluid (in meters per second), and u, v, and w are the components of $\boldsymbol{u}$ in $x-$, $y-$, and $z-$ directions; μ is the turbulent viscosity coefficient (in kilograms per meter second); P is the static pressure on the fluid microelement (in pascals); S_u, S_v, and S_w are the source items of momentum equation; S_T is the volume heat source item; k is the thermal conductivity of the fluid (in watts per meter kelvin); c is the specific heat capacity (in joules per kilogram kelvin)); and T is temperature (in kelvin).

The standard $k - \varepsilon$ model is adopted to simulate the turbulence in the model. The kinetic energy of turbulent flow k and the dissipation factor ε are introduced, and the following Boltzmann's equation referring to [19] is obtained. Combined with the solved region and operating conditions of the model this paper presents, the given boundary conditions are as follows.

1) S_1, the surface of rotor support that is not covered by horizontal disc air deflector, is the velocity inlet boundary of the coupling model. Air flow velocity at outlets of 12 heat exchangers is measured in the field test. The measured values are shown in Fig. 3; average flow velocity v_{ave} is computed as 2.68 m/s after excluding the singularity of measured data of No. 3 heat exchanger.

    We could obtain total circulation flow rate of cooling air $Q = v_{\text{ave}} \times S_{\text{he}} = 123.8 \text{ m}^3/\text{s}$, where S_{he} is the area of heat exchanger outlet. The inlet velocity of the coupling model is determined as $Q/S_{\text{inlet}} = 2$ m/s, where S_{inlet} is the area of rotor inlet.

2) S_2, the outlet surface of the solved region, which is the inlet of stator radial ventilation duct, is defined as the pressure outlet boundary. A simplified model is estab-

TABLE II
CALCULATED VALUES OF ADDITIONAL LOSSES

	P_{FeP} (kW)	$P_{2\nu k}$ (kW)	$P_{K\nu}$ (kW)
Calculated value	190.8	44.8	9.1
Design value	194.1	42.5	---

lished to determine the pressure value of outlet boundary of the calculation model. The region of simplified model, including stator and rotor, is within one-eighth of prototype in axial direction and a pair of rotors in circumferential direction. Outlets of stator ventilation ducts are defined as outlet boundary of this simplified model, and pressure value is set to 1 atm, namely, 101 325 Pa. After solving the simplified model, the pressure of the air-gap region is obtained as 101 722 Pa, and this pressure value is assigned to the pressure outlet boundary of calculation model.

3) Based on the circumferential symmetry of the generator, S_3, the surface at both sides of the model, is the periodic boundary.

4) The ambient temperature is 40 °C.

5) The rotor rotation drives cooling air to flow. The fluid rotational speed refers to the generator rated speed of 68.2 r/min.

6) The interfaces between cooling air and structural parts within the solved region are coupling surface conditions, and the remaining surfaces are considered as adiabatic surfaces.

C. Calculation of Losses in Rotor

For researching temperature field distribution of the rotor, the losses of different rotor parts are obtained from transient electromagnetic field calculation. The electromagnetic losses of the rotor include two parts, i.e., copper loss of the exciting winding and additional loss of magnetic pole surfaces and damper bars. The copper loss is calculated by I^2R, and the value is 558.1 kW. The additional loss is composed of three parts, including the additional loss of a magnetic pole surface under no-load rated voltage P_{FeP}, the rotor surface losses caused by stator windings' magnetomotive force (MMF) harmonic $P_{K\nu}$, and the additional loss caused by harmonic MMF of stator teeth on the magnetic pole surfaces and damper bars $P_{2\nu k}$. The calculation method and formula of additional loss are described in [20]. Calculated and design values of additional losses are given in Table II. The loss values are calculated for the generator under rated operation and applied to coupling model as heat sources in the fluid–thermal coupling analysis.

The flowchart of fluid–thermal coupling analysis is shown in Fig. 4. Solved region of the coupling model is determined according to symmetry of the prototype and requirement of the issue this paper focuses on. The solved region is meshed using 612 046 elements. The under-relaxation factors of pressure, momentum, k, ε, and energy are 0.3, 0.7, 0.8, 0.8, 1, respectively. The convergence criterion of continuity, velocity, k, and ε is 10^{-3}, and the convergence criterion of energy is 10^{-6}. The control equation (1) is solved using FLUENT solver after 146 iterations, thus obtaining air flow distribution and temperature distribution of rotor structures.
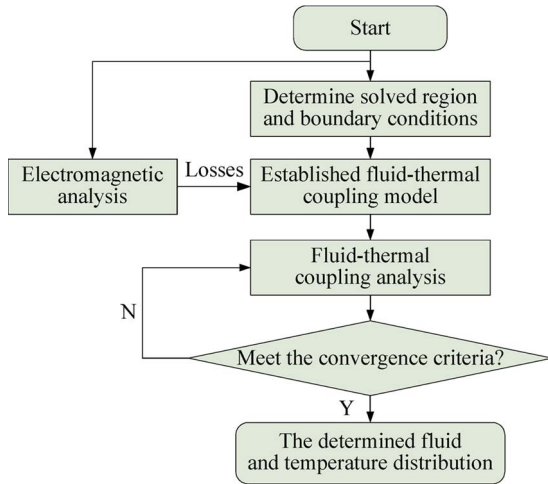
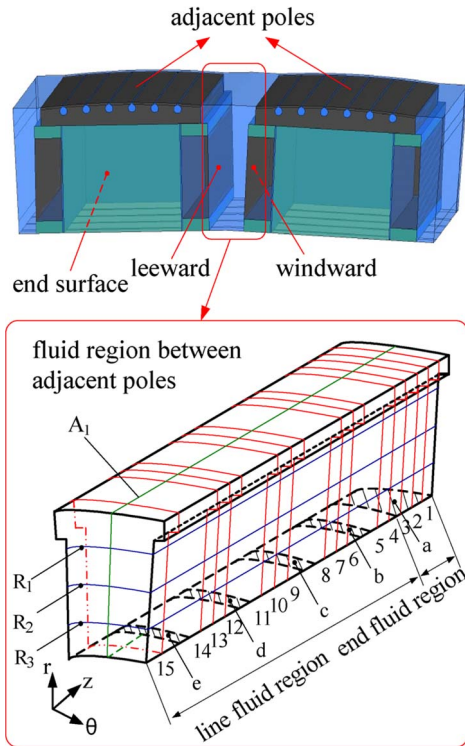Fig. 4. Fluid–thermal coupling analysis flowchart.

Fig. 5. Cross-sectional position diagram.

Fig. 6. Mass flow of rotor outlets.

Fig. 7. Velocity distribution of cooling air on axial plane A_1.

III. RESEARCH ON THE FLOW RULE OF COOLING AIR

The cooling air in the fully air-cooled hydrogenerator is always in turbulence state and has a very complex flow rule due to the rotor rotation. In order to study the impact of cooling air from rotor ventilation ducts in different axial positions on the flow condition of each other, it takes the axial cross sections from No. 1 to No. 15 from the end region toward the axial center in the interpole fluid region as the analysis positions.

Fig. 5 is a position diagram for the cross sections this paper involves during the analysis process. In Fig. 5, the red box refers to the fluid region between adjacent poles; "a" refers to the outlet of the fluid region at rotor ends, and "b," "c," "d," and "e" refer to the outlets of four ventilation ducts on the rotor yoke within half axial length of the generator. Axial
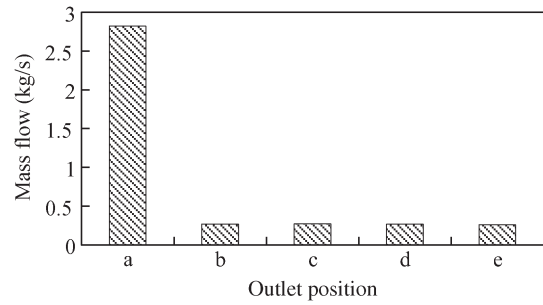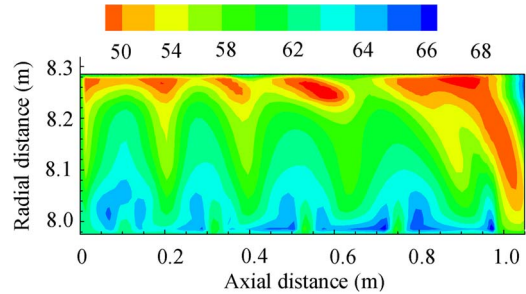
cross sections from No. 1 to No. 5 are located in the end fluid region; No. 6–8, No. 9–11, and No. 12–14 are three groups of axial equal distance cross sections in the interpole fluid region. R_1, R_2, and R_3 refer to the radial equal-distance cross sections of the interpole fluid region with their radii of 8.05, 8.13, and 8.21 m, respectively. According to the rotation direction of the generator, both sides of exciting winding could be determined as windward and leeward sides, respectively, as illustrated in Fig. 5. Plane A_1 locates in the central position of the interpole fluid region. The flow velocity component flowing toward the axial center is stipulated negative.

The cooling air first flows into the generator through the inlet of rotor support and then into the interpole fluid region through the end fluid region (outlet a) and rotor yoke ventilation ducts (outlets b–e). Fig. 6 shows the mass flow value of cooling air from a–e outlets. The mass flow of end outlet referring to a is 2.82 kg/s, accounting for 72.5% of the total circulation flow rate, whereas the mass flow of the ventilation duct outlets referring to b, c, d, and e is about 0.26 kg/s and the mass flow difference among the four outlets is relatively small. The high mass flow rate of end cooling air has a beneficial effect on the cooling of exciting winding ends, strengthening the dissipation conditions of exciting winding ends.

Fig. 7 shows the velocity distribution of cooling air on axial center plane A_1. The end flow velocity of cooling air is relatively high within the range of 62–70 m/s. The cooling air first flows radially into the region between poles, cools the exciting winding ends, and then flows into the axial center section at a relatively high flow velocity. The flow velocity of the ventilation duct outlets is within the range of 55–60 m/s, whereas the flow velocity between adjacent rotor yoke ventilation duct outlets is low. With the diffusion of cooling air, the flow velocity of cooling air gradually increases with the increasing direction of radius.
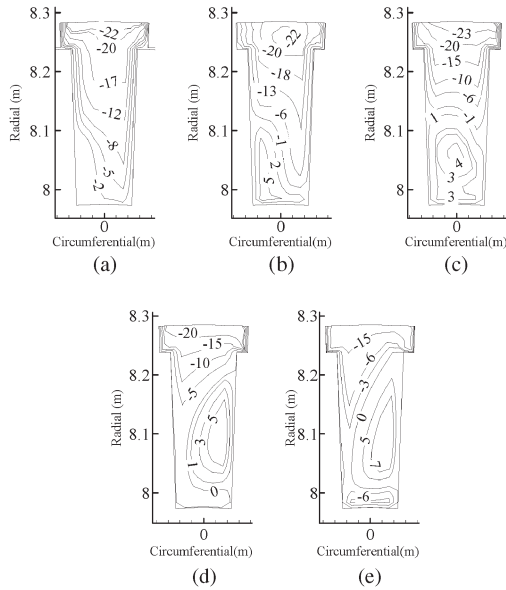
Fig. 8. Axial velocity component isogram of No. 1 to No. 5 cross sections (in meters per second). (a) No. 1 cross section. (b) No. 2 cross section. (c) No. 3 cross section. (d) No. 4 cross section. (e) No. 5 cross section.

In Fig. 8(a)–(e), an isogram is shown for the axial velocity component of No. 1 to No. 5 cross sections in the end fluid region. No. 1 cross section is located closely to the end of the established model. The axial velocity of cooling air in No. 1 cross section is negative with the maximum value of 22 m/s, and the axial velocity value gradually increases from the interpole bottom toward the top. The air flows into the end region through the rotor support and then flows axially at a relatively high velocity. However, affected by outlet b of rotor ventilation duct, the range of positive velocity values at the bottom of No. 2 to No. 5 cross sections gradually expands when the air flows toward the axial center. In other words, after the cooling air from two paths interacting with each other in the interpole bottom region, the cooling air that originally flows toward the axial center reflows toward the ends. The positive value of axial velocity increases from 5 to 8 m/s with the air flowing from No. 2 to No. 5 cross sections, whereas the negative velocity value in the interpole top region remains around 20 m/s, which decreases a little.

No. 6, No. 7, and No. 8 cross sections are located between b and c rotor ventilation duct outlets, and the air flow rule is affected jointly by cooling air out of b and c, as well as the end fluid. Fig. 9(a)–(c) shows the isograms for the axial velocity of No. 6 to No. 8 cross sections. No. 6 cross section is affected to the most extent as it is close to b ventilation duct. The air flows toward the axial center in No. 6 cross section. However, the positive velocity value region gradually forms on the windward (the right side of isogram is the windward, whereas the left side is the leeward) between poles with the advancement of No. 6, No. 7, and No. 8 cross sections toward the axial center. In other words, after the collision of the air flowing from two paths, a small part of air reflows toward the ends with the velocity value of 3 m/s. Compared with No. 1 to No. 5 cross sections, No. 6 to No. 8 cross sections reduce its interpole top axial velocity from 22 to 13 m/s.
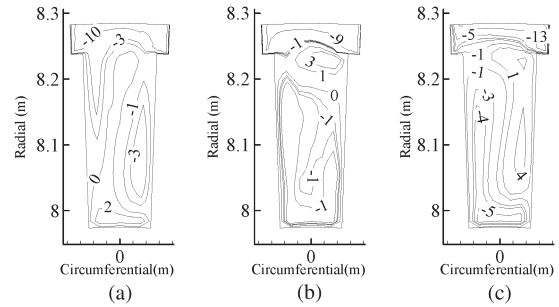

Fig. 9. Axial velocity component isogram of No. 6 to No. 8 cross sections (in meters per second). (a) No. 6 cross section. (b) No. 7 cross section. (c) No. 8 cross section.
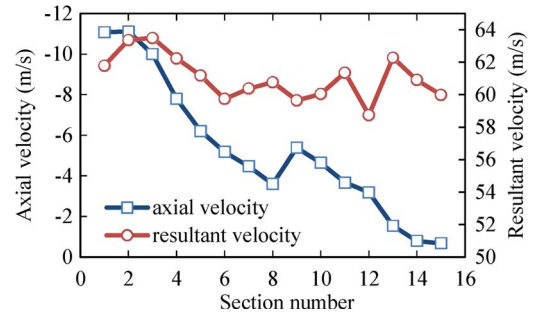

Fig. 10. Average velocity value of the fluid between poles.

Comparative studies are also made on No. 9 to No. 11 cross sections and No. 12 to No. 14 cross sections. The variation tendencies of air flow in these cross sections are consistent with those in No. 6, No. 7, and No. 8 cross sections.

Fig. 10 shows the average value of axial velocity and resultant velocity of air in No. 1 to No. 15 cross sections. Despite the different flow directions of the cooling air in various cross sections, the overall axial flow trend is toward the axial center and the average velocity value toward the axial center takes on a gradually decreasing tendency, i.e., the axial velocity in the cross section close to the ends is relatively high, and the average value of axial velocity gradually decreases toward the axial center. The average value of resultant velocity in various cross sections varies within the range of 58.7 to 63.5 m/s, thus concluding that the variation range is small.

Fig. 11(a)–(c) refers to the resultant velocity isograms of radial cross section $R_1 - R_3$ in the interpole fluid region. Fig. 11(a) illustrates the flow velocity distribution of R_1 at the radius of 8.052 m, and it takes on an obvious gradient change in the rotor yoke ventilation duct outlets and the end region close to the windward, which is the same as the variation rule of axial velocity in the axial cross section. During the early period when the cooling air goes between poles, the flow velocity of exciting winding bottom varies intensively on the windward with the maximum velocity value of 70 m/s. The velocity varies slowly on the leeward and is relatively evenly distributed. With the diffusion of cooling air along the radial height, the variation tends to be mild and slow on the windward and leeward but remains a relatively large gradient change in the end region. The flow velocity does not decrease, maintaining the maximum value at 70 m/s. Air flow velocity in R_3 at the radius of 8.211 m is more evenly distributed. Seen from the isogram, the velocity in the cross section remains stable within the range of 60 to 70 m/s, and the velocity difference between the windward and leeward
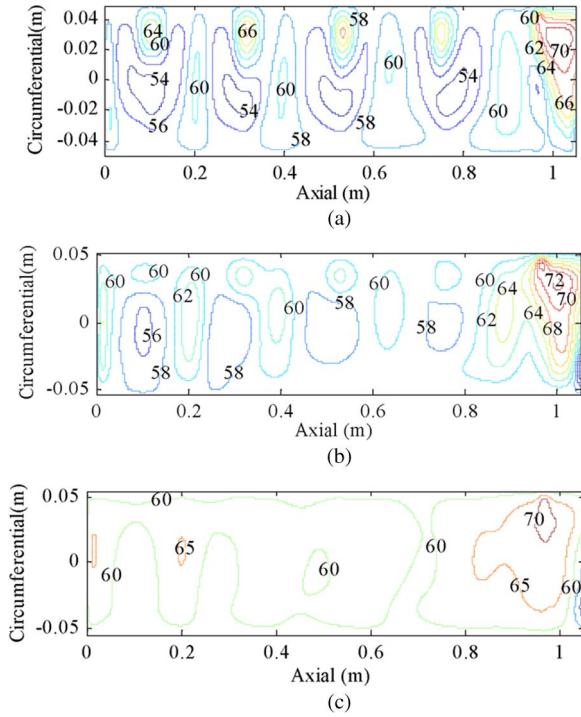
Fig. 11. Flow velocity isograms of radial cross section R_1-R_3 (in meters per second). (a). Radial cross section R_1. (b). Radial cross section R_2. (c) Radial cross section R_3.
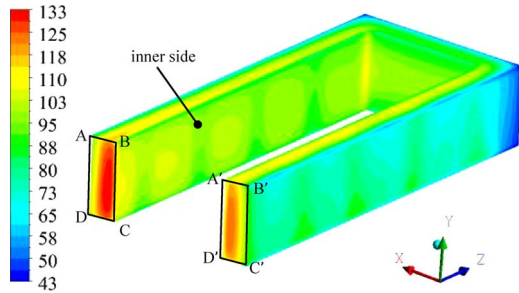

Fig. 12. Temperature distribution of exciting winding (in degrees Celsius).

decreases gradually. The velocity at the interpole top is always high due to the impact of the end fluid of high mass flow.

IV. TEMPERATURE FIELD ANALYSIS AND EXPERIMENTAL VERIFICATION

One of the main faults of hydrogenerator rotor is that the excessive local temperature rise of the hydrogenerator's exciting windings leads to the interturn insulation aging, thus resulting in the interturn short-circuit fault.

This paper obtains the temperature distribution of exciting windings through the calculations of coupling model. Fig. 12 shows the temperature distribution of exciting winding. Its temperature distribution takes on a gradually decreasing tendency from the center to the end. The maximum temperature of 132 °C appears in the leeward axial center plane A–B–C–D of the exciting winding, which resulted from the poor thermal dissipation condition of smaller mass flow of cooling air in the axial center of the machine. The temperature of leeward inner side of exciting winding is relatively high because it can only be cooled by conducting the thermal dissipation among

iron core, pole insulation, and the exciting winding itself. The temperature range of the inner side is 77 °C–116 °C. The maximum temperature difference of the windward axial center plane A–B–C–D and the leeward plane A′–B′–C′–D′; of exciting winding is 8 °C.

There is a certain difficulty in temperature measurement of a large hydrogenerator at a rating of megawatts. The resistance testing method is widely adopted for temperature measurement of exciting winding and determines the average temperature according to the relationship that the resistance varies correspondingly with the temperature variation. Voltage and current transducers are used to obtain the resistance of exciting winding. The relationship between temperature rise and resistance could be determined as [21]

$$\theta = \frac{R_2 - R_1}{R_1}(K + t_1) + t_1 - t_2$$
$$R = \frac{\left[U_f - L_f\left(\frac{\mathrm{d}I_f}{\mathrm{d}t}\right) - U_B - I_f(R_B + R_l)\right]}{I_f} \quad (2)$$

where R_2 is the winding hot resistance (in ohms), t_2 is the cooling medium temperature corresponding to R_2, R_1 is the winding resistance under the cold state (in ohms), t_1 is the winding temperature corresponding to R_1, and K is a constant; for copper winding, it is 235, U_f is the exciting voltage (in volts), I_f is the exciting current (in amperes), L_f is the inductance of exciting winding, U_B is the voltage drop of carbon brush (in volts), R_B is the resistance of carbon brush (in ohms), and R_l is the resistance between measuring point and carbon brush (in ohms).

The temperature rise of exciting winding could be obtained via the winding resistance at cold state (measured before generator running) and hot state (measured after generator running at rated state). A field test of temperature measurement is performed on this 250-MW fully air-cooled hydrogenerator operating at Wuqiangxi Hydropower Station, which is manufactured by Harbin Electric Machinery, getting the measured average temperature of exciting winding as 108.6 °C. The average temperature of exciting winding calculated by the coupling model is 106 °C, which could be determined as

$$T_{\mathrm{ave}} = \frac{1}{V}\sum_{i=1}^{k} T_i V_i \quad (3)$$

where T_{ave} is the average temperature (in degrees Celsius), V is the exciting winding volume (in cubic meters), T_i is the temperature of element within exciting winding (in degrees Celsius), and V_i is the element volume (in cubic meters).

The computed error between the calculated and measured values is 2.4%, thus verifying the accuracy of the calculation model and solution method in this paper.

By equipping the rotor pole with damper bars, the free rotor oscillation can be inhibited and the capacity of the generator to undertake the unsymmetrical load can be enhanced. In terms of the hydrogenerator with a requirement for frequent starts and stops in a power system, the faults that the damper bars are broken or thrown out of slots often occur under the action of thermal stress. Heat-transfer coefficient is a key factor characterizing thermal dissipation condition. This paper makes
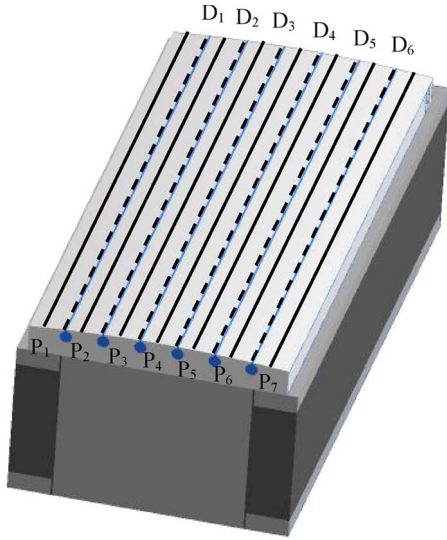
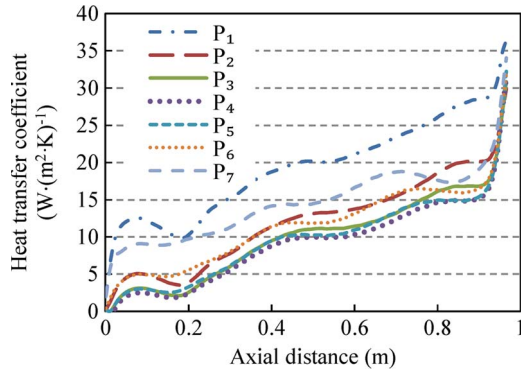Fig. 13.   Location of the sample lines on a rotor pole.

Fig. 14.   Heat-transfer coefficient of P_1-P_7 on the pole shoe surface.

an analysis of heat-transfer coefficient of damper bars and pole shoe surfaces. Heat-transfer coefficient could be determined as

$$h = \frac{q}{T_{\text{wall}} - T_{\text{ref}}} \tag{4}$$

where, q is the heat flux (in watts per square meter), T_{wall} is the structure wall temperature (in kelvin), and T_{ref} is the average temperature of cooling air (in kelvin).

Take seven equidistant axial sampling lines P_1-P_7 on the pole shoe surface along the direction of rotation from the windward to the leeward and six sampling lines D_1-D_6 from damper bars of a rotor pole. Fig. 13 gives the location of the sample lines P_1-P_7 and D_1-D_6. The distributions of the heat-transfer coefficient of sampling lines on the pole shoe and damper bar surfaces are illustrated in Figs. 14 and 15.

The heat-transfer coefficient of pole shoe surface takes on a gradually increasing tendency from the axial center toward the ends and significantly increases at ends under the action of the high velocity of cooling air. The heat-transfer coefficient of the first sampling line close to the windward is higher than that of other sampling lines in the same axial positions with the maximum value of the former of $36.4 \, \text{W} \cdot (\text{m}^2 \cdot \text{K})^{-1}$. The heat-transfer coefficient of No. 7 sampling line closest to the leeward remains at a high level. After an overview of the positions from No. 1 to No. 7 on the pole shoe surface, it is found that the heat-transfer coefficient on both circumferential sides of pole shoes
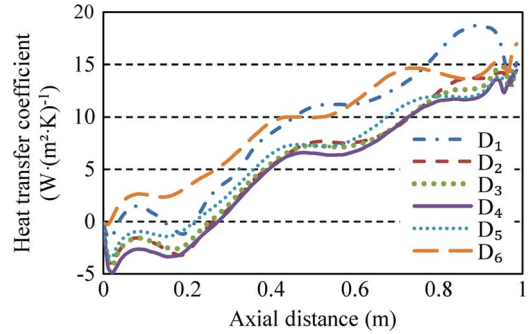

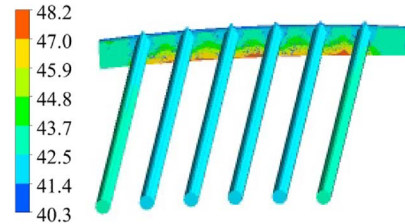Fig. 15.   Heat-transfer coefficient of D_1-D_6 on the damper bar surface.

Fig. 16.   Temperature distribution of damper bars and end ring (in degrees Celsius).

is higher than that in the middle position, whereas the heat-transfer coefficient in the axial center is lower than that at ends. The distribution rule of heat-transfer coefficient of the damping bar position is the same as that of the pole shoe surface, and the maximum value is $18.7 \, \text{W} \cdot (\text{m}^2 \cdot \text{K})^{-1}$.

Fig. 16 is a diagram for the temperature distribution of damper bars and end ring, where the average temperature of damper bars is $42.3 \, °\text{C}$, whereas the average temperature of end ring is $42.0 \, °\text{C}$. The inner surface of the end ring can only proceed with thermal conduction through the pole pressure plate it contacts due to its relatively poor thermal dissipation condition, thus reaching a relatively high temperature of $48.2 \, °\text{C}$; the temperature distribution of six damper bars is more even. The temperature of the two damper bars located in the middle is slightly lower than that of the damper bars on both sides. The axial temperature of every damper bar tends to be consistent because of the better thermal conductivity of copper materials.

V. CONCLUSION

This paper has calculated the distribution of fluid and temperature fields through the establishment of a 3-D fluid–thermal coupling model for a fully air-cooled fanless hydrogenator rotor. The following conclusions can be obtained.

1) The cooling air that flows into the rotor end region and then into the region between poles through the horizontal disc air deflector accounts for 72.5% of total mass flow rate. The cooling air of high mass flow at ends has a beneficial effect on cooling end exciting windings.

2) As there is cooling air of high mass flow at ends, the air at the interpole top flows toward the axial center, thus improving the cooling conditions of the axial center of the generator. The axial velocity gradually decreases from the ends toward the axial center section.

3) It is prone to a turbulent vortex on the windward side. The back-flow phenomenon toward the generator end region generally occurs on the windward of exciting windings. Due to the rotor rotation and Coriolis force, the high-wind-speed region of the cooling air on the pole shoe surface gradually shifts from the windward toward the leeward.

References

[1] S. Y. Fan, "Analysis of stability for large and medium-sized hydro-generating unit," in *Proc. CSEE*, Mar. 2012, vol. 32, pp. 140–148.

[2] R. Romary, C. Demian, P. Schlupp, and J. Y. Roger, "Offline and online methods for stator core fault detection in large generators," *IEEE Trans. Ind. Electron.*, vol. 60, no. 9, pp. 4084–4092, Sep. 2013.

[3] G. Traxler-Samek, R. Zickermann, and A. Schwery, "Advanced calculation of temperature rises in large air-cooled hydro-generators," in *Proc. 18th ICEM*, Sep. 6–9, 2008, pp. 1–6.

[4] D. A. Staton and A. Cavagnino, "Convection heat transfer and flow calculations suitable for electric machines thermal models," *IEEE Trans. Ind. Electron.*, vol. 55, no. 10, pp. 3509–3516, Oct. 2008.

[5] C. Mejuto, M. Mueller, M. Shanel, A. Mebarki, and D. Staton, "Thermal modelling investigation of heat paths due to iron losses in synchronous machines," in *Proc. IET Power Electron., Mach. Drives Conf.*, Apr. 2008, pp. 225–229.

[6] H. Gorginpour, H. Oraee, and R. A. McMahon, "Electromagnetic thermal design optimization of the brushless doubly-fed induction generator," *IEEE Trans. Ind. Electron.*, vol. 61, no. 4, pp. 1710–1721, Apr. 2014.

[7] C. Shiyuan, "Network analyses of ventilation system for large hydrogenerator," in *Proc. 5th ICEMS*, Aug. 18–20, 2001, vol. 1, pp. 137–140.

[8] F. Zhou, W. L. Li, Y. P. Hou, and S. C. Cheng, "3D nonlinear steady-state temperature field after stator winding insulation laminating for large hydro-generator," in *Proc. 5th ICEMS*, Aug. 18–20, 2001, vol. 2, pp. 1149–1152.

[9] F. Y Huo, W. L. Li, and Y. Zhang, "Calculation of damper winding loss and influence on large hydro-generator temperature," in *Proc. ICCASS*, Oct. 22–24, 2010, vol. 4, pp. 365–369.

[10] W. L Li, S. Y. Ding, H. Y. Jing, and Y. L. Luo, "Numerical calculation of multicoupled fields in large salient synchronous generator," *IEEE Trans. Magn.*, vol. 43, no. 4, pp. 1449–1452, Apr. 2007.

[11] S. Stipetic, M. Kovacic, Z. Hanic, and M. Vrazic, "Measurement of excitation winding temperature on synchronous generator in rotation using infrared thermography," *IEEE Trans. Ind. Electron.*, vol. 59, no. 5, pp. 2288–2298, May 2012.

[12] A. Boglietti *et al.*, "Evolution and modern approaches for thermal analysis of electrical machines," *IEEE Trans. Ind. Electron.*, vol. 56, no. 3, pp. 871–882, Mar. 2009.

[13] C. Buccella, C. Cecati, and F. de Monte, "A coupled electrothermal model for planar transformer temperature distribution computation," *IEEE Trans. Ind. Electron.*, vol. 55, no. 10, pp. 3583–3590, Oct. 2008.

[14] F. Marignetti and V. Delli Colli, "Thermal analysis of an axial flux permanent-magnet synchronous machine," *IEEE Trans. Magn.*, vol. 45, no. 7, pp. 2970–2975, Jul. 2009.

[15] M. Popescu, D. Staton, D. Dorrell, F. Marignetti, and D. Hawkins, "Study of the thermal aspects in brushless permanent magnet machines performance," in *Proc. WEMDCD*, Mar. 11–12, 2013, pp. 60–69.

[16] C. Jungreuthmayer *et al.*, "Heat and fluid flow analysis of an internal permanent magnet synchronous machine by means of computational fluid dynamics," in *Proc. IEMDC*, May 15–18, 2011, pp. 515–520.

[17] P. H. Connor *et al.*, "Computational fluid dynamics modelling of an entire synchronous generator for improved thermal management," *IET Elect. Power Appl.*, vol. 7, no. 3, pp. 231–236, Mar. 2013.

[18] D. Staton, A. Boglietti, and A. Cavagnino, "Solving the more difficult aspects of electric motor thermal analysis in small and medium size industrial induction motors," *IEEE Trans. Energy Convers.*, vol. 20, no. 3, pp. 620–628, Sep. 2005.

[19] H. K. Versteeg and W. Malalasekera, *An Introduction to Computational Fluid Dynamics: The Finite Volume Method*. Upper Saddle River, NJ, USA, 2007, pp. 72–78.

[20] W. L. Li, Y. Zhang, and Y. H. Chen, "Calculation and analysis of heat transfer coefficients and temperature fields of air-cooled large hydro-generator rotor excitation windings," *IEEE Trans. Energy Convers.*, vol. 26, no. 3, pp. 946–952, Sep. 2011.

[21] Y. N. Bai, *Design and Calculation of Hydro-Generator*. Beijing, China: Beijing Mech. Ind. Press, 1982, pp. 808–810.

Shukuan Zhang was born in Harbin, China, in 1988. He received the B.S. and M.S. degrees in electrical machinery and appliances from Harbin University of Science and Technology, Harbin, in 2011 and 2014, respectively. He is currently working toward the Ph.D. degree at Harbin Institute of Technology, Harbin.

His research interests include electromagnetics, fluids, and thermal analysis of large power electrical generators and permanent-magnet machines.

Weili Li was born in Harbin, China, in 1962. He received the Master's degree from Harbin Institute of Electrical Technology, Harbin, in 1993 and the Ph.D. degree from the Russia Electric Power Research Institute, Moscow, Russia, in 1997.

He is currently a Professor with the School of Electrical Engineering, Beijing Jiaotong University, Beijing, China. He is the author or coauthor of more than 200 published refereed technical papers, and he also holds more than 20 patents. His research interests include research on synthesis physical fields of large electrical machines and special electrical machines.

Prof. Li is an Editorial Board Member of the *Journal of Electric Machines and Control*.

Jinyang Li was born in Harbin, China, in 1994. He is currently working toward the B.S. degree in electrical engineering and automation in the School of Electrical Engineering and Automation, Harbin Institute of Technology, Harbin.

Likun Wang was born in Harbin, China, in 1987. He received the B.Sc., M.Sc., and Ph.D. degrees from Harbin University of Science and Technology, Harbin, in 2010, 2013, and 2015, respectively, all in electrical machinery and appliances.

He is currently a Lecturer at Harbin University of Science and Technology. He has authored or coauthored seven refereed technical papers in IEEE Transactions and one book, and he holds several patents. His research interests include electromagnetics, fluids, and thermal analysis of large power electrical machines, particularly large turbo-generators. He also conducts research on coordinate theory of generators and power grids and performance prediction and optimization for electrical machines.

Mr. Wang was awarded the Outstanding Graduate of Heilongjiang Province in 2013 and the National Scholarship for Doctoral Candidates in 2012 and 2014.

Xiaochen Zhang (S'09–M'12) received the Master's degree from Harbin University of Science and Technology, Harbin, China, in 2006 and the Doctor's degree from Harbin Institute of Technology, Harbin, in 2012.

He is currently with the School of Electrical Engineering, Beijing Jiaotong University, Beijing, China. His research interests include electromagnetic and thermal analysis of electrical machines, particularly permanent-magnet machines.